On the competition of laser acceleration mechanisms of electrons and ions in steep density profiles at overdense plasmas interfaces

Stefan Hüller, Anna Porzio, Anne Héron, Patrick Mora

On the competition of laser acceleration mechanisms of electrons and ions in steep density profiles at overdense plasmas interfaces

S. Hüller,[1] A. Porzio,[2,1] A. Héron,[1] and P. Mora[1]
[1)] *Centre de Physique Théorique(CPHT), CNRS, Ecole Polytechnique, IP Paris, 91128 Palaiseau, France*
[2)] *LAGA, Institut Galilée, Université Paris 13, Villetaneuse, France*

The role of the density gradient in the electron acceleration process by intense laser pulses for a plasma profile with a steep interface between vacuum and a strongly overdense plasma is investigated based on particle-in-cell simulations with the EMI2D code. Laser pulses at relativistic intensities interacting with finite gradients at the laser-plasma interface favour the formation of an electron cloud and collective electron motion in the underdense plasma provided that the pulse duration is long enough to form a standing wave structure. It is shown that the steepness of the gradient has an influence on the evolution of the distribution of electrons that are injected into the dense plasma. Heating mechanisms of the electron bulk and of a very energetic electron tail are identified. The heating of the targets evolves almost step-wise each time when bunches of electrons accelerated to relativistic energies return to the laser-plasma interface. The heating dynamics depending on the gradient at the laser-plasma interface has consequences on the acceleration of the ion front at the rear of the target. This is elaborated by determining the predominant hot electron populations and their temperature which governs the expansion of the rear density profile. The role of the temporal dynamics of the hot electron temperature is investigated with respect to the known analytic models for ion acceleration. It is shown then that the ion dynamics can still be quite well reproduced with models provided that the hot electron population be traced in determining its temperature and density.

14 February 2024

I. INTRODUCTION

Ultra-intense laser pulses that impinge on a dense plasma target can accelerate electrons to highly relativistic energies such that they can penetrate into a dense target. When those electrons arrive at the rear face of the dense target, rarefaction of the plasma profile[1,2] and strong charge separation effects[2,3] lead to the acceleration of the plasma ions. The ion acceleration process depends on the efficiency of the conversion of the laser energy into electron heating, and, according to models[2–9] on the temperature of the hot electron tail of the distribution. Imprint of micro structure and/or of the excitation of surface modes on the dense target surface has been investigated to improve the conversion efficiency in order to inject electrons into the dense plasma. In recent work by Héron et al.[10] it was found that a density gradient at the interface where the intense laser pulses impinges on the dense target may act favourably for conversion in kinetic energy. While today electron acceleration is considered in the relativistic laser intensity regime, the latter process is well known already from the non-relativistic regime, even related to wave conversion processes, both in their linear and non linear stage[11–13].

Heating of electrons is known from the 1970's via resonance absorption, mostly for the case of obliquely incident and p-polarized laser light for the case of non-relativistic intensities[11,12]. At higher intensity, and in particular when profile steepening arises, other processes come into play[13]. For the case of relativistic laser intensities, with a pre-plasma in front of the critical density, the electron acceleration has been revisited later by Kemp et al.[14], taking into account ponderomotive profile steepening and ponderomotive heating of the electrons.

In this article we focus on the production of a hot electron population and the acceleration of ultra-relativistic electrons around a steep laser-plasma interface. We give particular attention to the role of the plasma profile on the acceleration of ions at the rear of the target due to the modification electron distribution by those laser-induced electron heating mechanisms. The laser pulses considered have a duration such that a standing wave structure forms in front of the target due to partially reflected light.

The results presented are based on particle-in-cell (PIC) simulations with the code EMI2D developed by J. C. Adam and A. Héron at CPHT, in a version with 2 dimensions in the configuration- and 3 in momentum space (2D3V). The simulation configurations are based on target of thickness between $150k_0^{-1}$ and $300k_0^{-1}$ and width of $27k_0^{-1}$. Simulation run times last up to $2000\omega_0^{-1}$, corresponding to 800-1000fs for frequencies ω_0 of lasers wave lengths in the range 0.8-1μm, such that relativistic electrons emitted at the interface can, a priori, return up to two times from the rear face of the target.

The interactions in such configurations are complex, with respect to both the effects along the target surface and the effects inside the dense target with return current effects and magnetic field generation[15], we concentrate here on the electron and ion motion, as well as of the fields in the direction of laser propagation, with normally incident laser light. In the majority, the results are presented in the spatial average over the dimension y perpendicular to the laser axis.

In a preceding publication[16] we have shown that the multi-dimensional aspect is crucial for the production

of energetic electrons for intense laser pulses. In this article we have shown that energetic electrons ejected from the laser-dense plasma interface into the direction of the incoming laser are subject to successive stochastic acceleration[17–19]. Stochastic acceleration is explained by the non linear motion in the standing wave field[20,21] formed by the incident and reflected light. In first approximation, this acceleration process can be simplified to 1D geometry. However, the light fields do not have a plane wave structure due to upcoming filamentation which is eventually the reason why a certain population of energetic electrons can be ejected into the vacuum region, otherwise impossible in 1D geometry[22,23].

While in this preceding work we have initially considered an abrupt density jump, we investigate here aspects that appear when the plasma density gradient is finite. The latter can be characterized by the electron density gradient length $L_g = (n_e/\partial_x n_e)|_{n_e=n_c}$ at critical density n_c where the plasma frequency, ω_{pe} equals the laser frequency, i.e. $\omega_0 \equiv \omega_{pe}(n_e = n_c)$. Kemp et al. in Refs. 14 and 24 underline that the physics at the interface change considerably in presence of a pre-plasma which appears intrinsically with a finite density gradient. Although ponderomotive profile steepening will dynamically limit the gradient L_g^{-1} at critical density, an underdense "foot" of electron population will result in collective oscillations of those electrons in the superposed (incident and reflected) light field. As explained in what follows, only a small portion of the electrons in such a pre-plasma are super-relativistic, such that the resulting heating process is different from stochastic acceleration.

Our article is organized as follows: in the first section, after defining the configurations of the plasma profiles used, we illustrate via phase space snap shots from PIC simulations and the resulting distribution functions the essential features of acceleration processes in comparing plasma profiles with an abrupt jump up to $100n_c$ (k_0L_g =0) with profiles having a finite gradient k_0L_g =1 or 3. In the section on the ion acceleration at the rear of the target, we elaborate the features of the electron and ion distribution functions essential for the rarefaction of the profile. We compare furthermore the evolution of the outgoing ion front with theoretical models, before concluding with discussions.

II. EMI2D SIMULATIONS

A. Simulation set up

We have performed simulations with the PIC code EMI2D with a laser pulse with a ramp in time that reaches its maximum intensity after $\omega_0 t = 100$, keeping this maximum value until the end of the simulation. The simulation boxes have a width of $27k_0^{-1}$ and a length of $550k_0^{-1}$ or $800k_0^{-1}$ for the target thickness of $150k_0^{-1}$ or $300k_0^{-1}$, respectively. For the relatively small box width, the incoming laser light is modeled by an incoming plane wave. The components of the electromagnetic field solver are E_x, E_y, and B_z, hence two-dimensional (2D, x,y) geometry, while the particle motion is 2D in configuration space (x,y), but three-dimensional (3V) in momentum space, allowing for the components p_x, p_y, p_z for the electrons, $v_{i,x}$, $v_{i,y}$, $v_{i,z}$ for (here non-relativistic) ions. Periodic boundary condition are assumed in the direction perpendicular to the incoming laser light.

The intensity value applied corresponds to a normalized vector potential amplitudes a_0 [$= eE_L/(m_e\omega_0)$] = 2.8. The plasma interface situated around $150k_0^{-1}$ reflects the incoming laser light such that for $\omega_0 t >$150 potentially a standing wave structure between incident and reflected light fields starts to form. The thickness of the target was chosen such that only fast particles can transverse the bulk, but no fields, namely between $150k_0^{-1}$ and $300k_0^{-1}$. Rarefaction on both sides remains uncoupled over the simulation duration. The simulations were performed with mobile ions, without applying collisions, in a hydrogen plasma with an initial electron thermal speed of $v_{th,e}$ =0.03c (T_e = 230eV) and an ion/electron temperature ratio of T_i/T_e =0.1.

Outgoing particles (electrons) are replaced by incoming ones; their momentum is conserved.

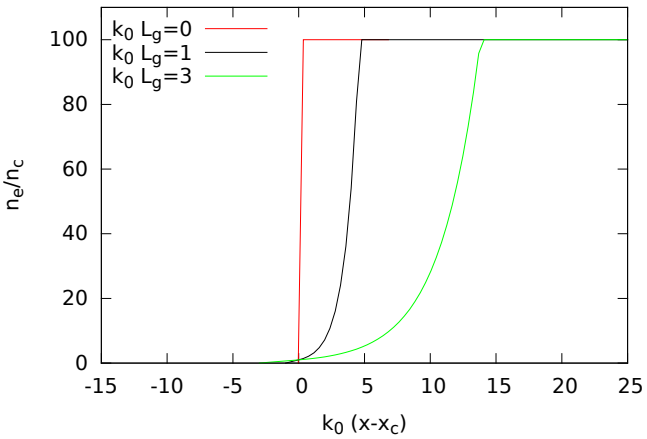

FIG. 1. Density profiles n_e/n_c as a function of x at the plasma interface for three different gradient lengths L_g at the critical density following the profile shape following Eq. (1).

B. Pre-plasma formation: step profile vs. gradient

Figure 1 illustrates the front profiles chosen at the plasma interface, with a step-like shape, up to $n_{\max}$ (here $100n_c$) and, alternatively exponentially increasing profiles between $n_e = n_c$ and $n_{\max}$, for which a linear ramp has been chosen for lower densities, as defined by

$$\frac{n_e(x)}{n_c} = \begin{cases} 0 & \text{for } x-x_c < -L_g, \\ 1+\frac{x-x_c}{L_g} & \text{for } -L_g < x-x_c < 0, \\ e^{(x-x_c)/L_g} & \text{for } 0 \le x-x_c < \log\frac{n_{\max}}{n_c}, \\ 100 & \text{for } x-x_c \ge \log\frac{n_{\max}}{n_c}\ , \end{cases} \quad (1)$$

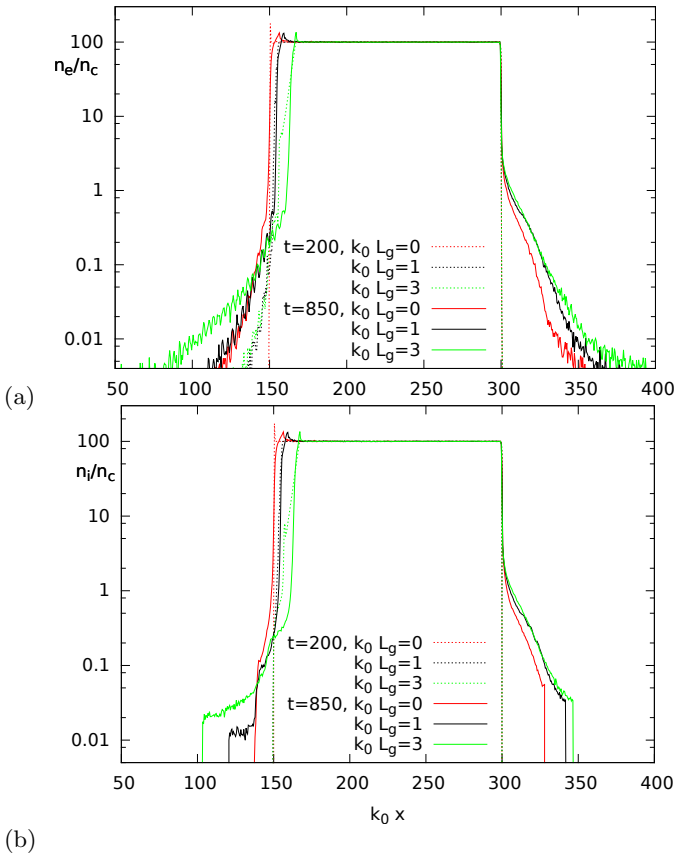

FIG. 2. (a) Electron and (b) ion density profiles n_e/n_c, averaged over y, as a function of x, for times $\omega_0 t$ =200 and 850 for three cases $k_0 L_g$ =0,1, and 3 (red, black, and green lines respectively) with x_c=150k_0^{-1} and thickness 150k_0^{-1}.

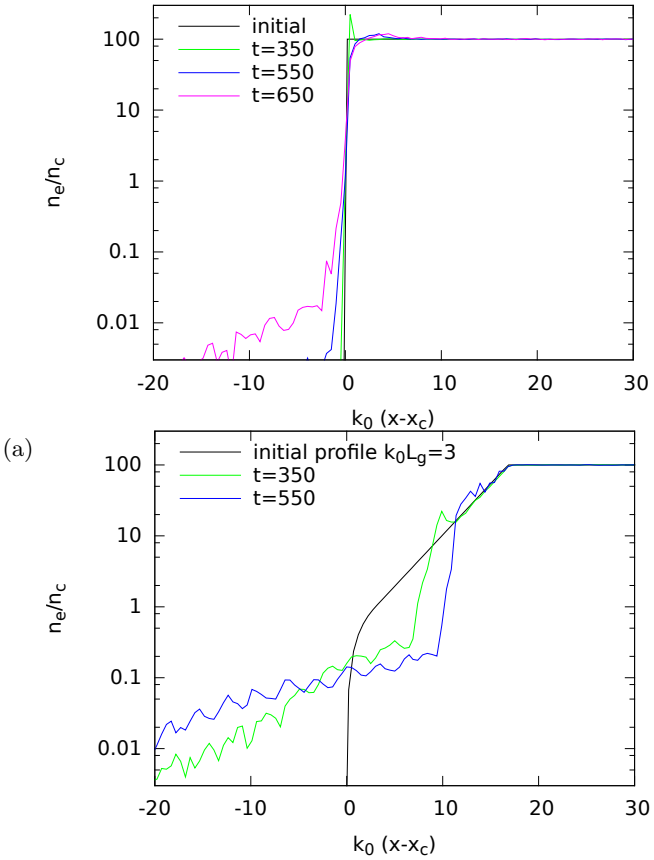

(b)

FIG. 3. Electron density profiles n_e/n_c, averaged over y, as a function of x, around the vacuum plasma interface at x_c=150, for three different times and for the cases (a) of an initially step-like profile ($k_0 L_g$ =0) and (b) of an initial exponential density profile density with $k_0 L_g$ = 3. A non-negligible pre-plasma at low density ($< 0.03 n_c$) forms lately, with a stronger spatial extension and density ripples for case (b).

with x_c denoting the position of the critical density n_c. The step-like profile corresponds hence to $L_g \to 0$.

The entire density profiles of electrons and ions (here charge $Z = 1$) are illustrated in Figs. 2, respectively, for three cases with initially different gradients, namely, $k_0 L_g = 0$ (red lines), $= 1$ (black), and $= 3$ (green), for two time instants, $\omega_0 t$ =200 (early, dashed lines) and =850 (solid lines). The values shown are averaged over the whole width of the second dimension y in the 2D simulation. While electron profiles are oscillatory (undulated: front) or noisy (rear), the ion profiles show a clear front of expansion on each side. Figures 3 illustrate how an initially step-like profile and how an exponential profile evolve with ongoing time. While the step-like profile keeps a very steep gradient around $x = x_c = 150 k_0^{-1}$ with $n_e(x_c) = n_c$, a low-density foot with $n_e < 0.1 n_c$ develops as pre-plasma for $x < x_c$. For the exponentially-shaped profile the low-density foot occurs at quite earlier and at higher densities. On the other hand, the initial gradient, here $L_g^{-1} = k_0/3$ steepens considerably and the position of the critical density is shifted towards higher values in x due to the light pressure.

C. Acceleration and heating in the steep front layer

As a consequence of the different profiles and absolute electron densities in the "pre-plasma" , the electron distribution function evolves with different temporal dynamics, related to the degree of reflected light, Figs. 4. The laser light is initially completely reflected, leading to a standing wave pattern in the pre-plasma, with a gradual decrease in the reflectivity R (defined as $\equiv |B_z(x = 0)/B_{z,in}|^2$) up to $\omega_0 \simeq 350$. During a transient period from $200 < \omega_0 t < 600$ the spectral content of the reflected signal exhibits also higher harmonics associated with non linear electron motion is seen in Fig. 5. The second, hence even harmonic only occurs for the case with an initial step-like interface, $k_0 L_g = 0$, at only for later times for $\omega_0 t > 1000$. Both the Figures 4 and 5 show after a transient period another drop in the reflectivity shortly after $\omega_0 t = 600$. With this decrease in reflectivity from $R > 85\%$ to $R \simeq 70\%$, the uneven

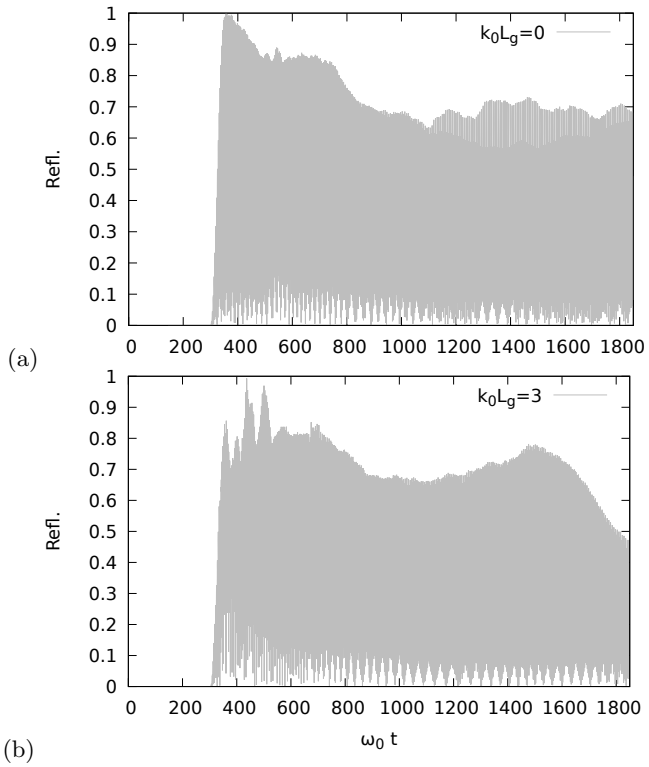

FIG. 4. Time evolution of the reflected light flux for the cases $k_0 L_g = 0$ (top) and $= 3$(bottom). The onset time of $\omega_0 \sim 200$ corresponds to twice the propagation time of the incoming laser pulse to reach the interface. .

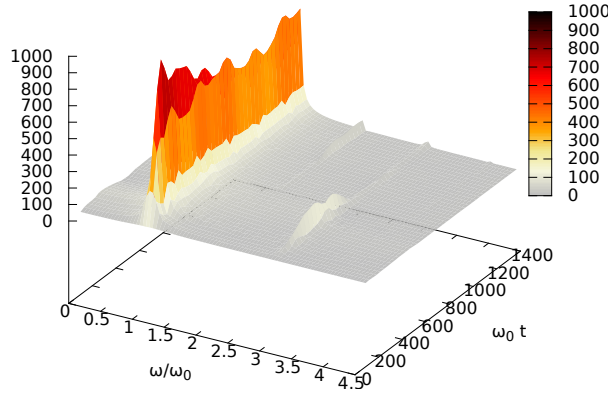

FIG. 5. Time evolution of the reflected light flux, spectrally analyzed for the case $k_0 L_g = 0$ as a function of time and of the frequency in multiples of the laser frequency. The onset time of $\omega_0 t \sim 300$ corresponds to twice the propagation time of the incoming laser pulse to reach the interface. The amplitude unit of ~ 900 corresponds to 100% reflection in Fig. 4. .

harmonics drop considerably. Phase space snapshots of the electron momenta p_x versus x, are illustrated respectively, in Figs. 6 7 for the cases of a step-like profile and a profile with gradient, namely $L_g = 3k_0^{-1}$, respectively, both taken at similar times. The color bars for the phase space contours are chosen with the purpose to

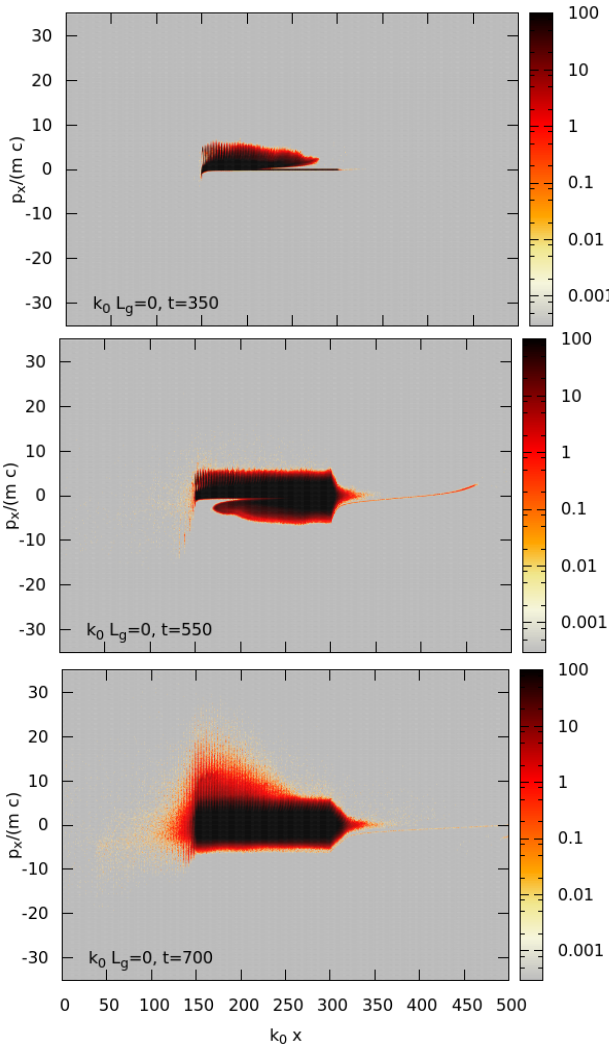

FIG. 6. Phase space contour snap shot in x-p_x, taken at $\omega_0 t$ =350, 550, and 700 (top, center, bottom) for the case of an initially step-like profile with $a_0 = 2.8$, x_c =$150k_0^{-1}$. The color map is highly saturated for >5000 in order to emphasize the population of high energy electrons.

highlight the essential physics in the front of the high density plasma bulk, the latter appearing in saturated dark colour. For both cases one can observe an undulation in the electron phase space contours following the standing wave pattern formed by the superposition of the incident laser field and the reflected light. The number of particles, consistent with the observation concerning Figs. 3, is higher for the case with gradient. In the x-p_x phase spaces a clear signature of the stochastic acceleration mechanism[17,18,22] can be identified, as worked out in our previous work[16], for which the momenta $|p_x|$ of energetic electrons are gradually increased each time with a change in sign of p_x. For the cases with a finite density gradient, the acceleration process proves to arise earlier in time so that energetic, but moderately relativistic electrons arrive earlier at the rear of the target. Those electrons consequently are redrawn earlier in the oppo-

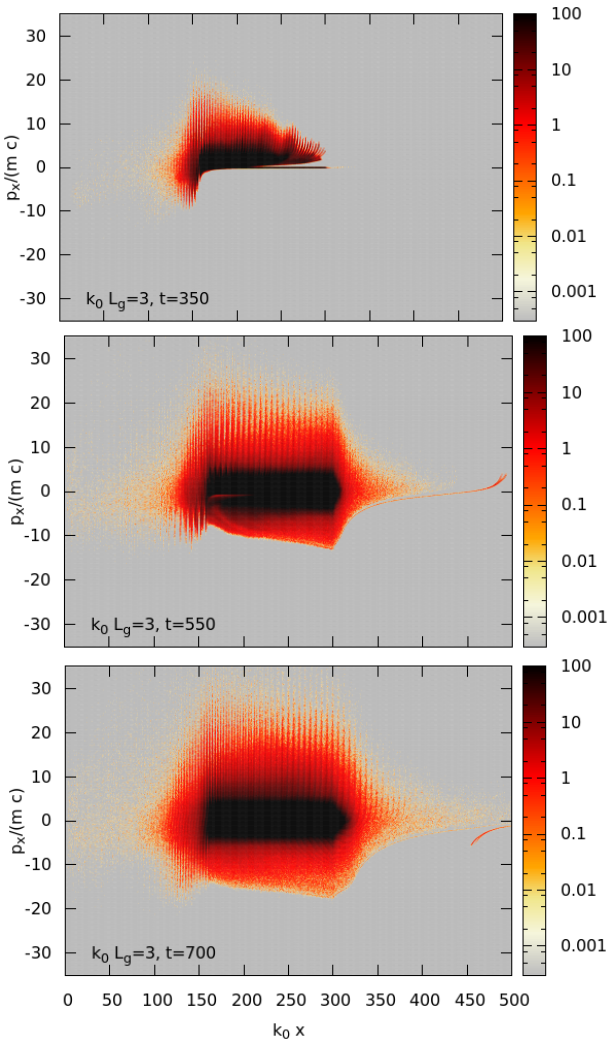

FIG. 7. Phase space contour snap shot in x-p_x, taken at $\omega_0 t$ =350, 550, and 700 (top, center, bottom)for the case of an initially exponential profile ($k_0 L_g$ = 3), both with a_0 = 2.8, x_c =150k_0^{-1}. The color map is highly saturated for >10 in order to emphasize the population of high energy electrons.

site direction. Kemp et al.[14,24] have studied in detail the heating process for such profiles by showing that a bulk heating occurs in the layer of the gradient, attaining a width associated with ponderomotive effects.

This bulk heating proves to be more efficient in presence of a gradient in front of the plasma interface. Those electrons can be identified by the width of the saturated (black color) bulk in the $x - p_x$ phase space in Fig. 7, which is more pronounced for the case $k_0 L_g$3 with respect to $k_0 L_g$ =0, which is also seen when inspecting instead the x-p_y phase space dominated by the electron quiver motion in the polarization direction of the laser fields, see Figs. 8. Another mechanism that can come into play only for gradients with a sufficient gradient length $L_g > 0$, is the mechanisms for a thin layer[25] in the vicinity of the skin depth.

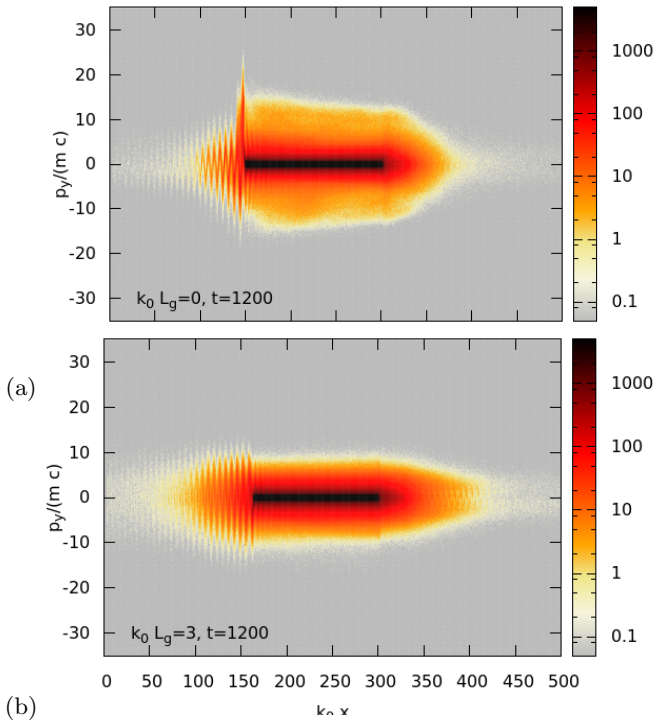

FIG. 8. Phase space contour snap shots in x-p_y for the cases (a, top) $k_0 L_g$ = 0 and (b, bottom) $k_0 L_g$ =3 taken at $\omega_0 t$ =1200. The color map is highly saturated for >5000 in order to emphasize the population of high energy electrons.

D. Electron distributions

The acceleration mechanisms observed in the front layer, depending on the profile gradient, have consequences on the electron distribution functions. To illustrate this, we have determined the distribution densities for both $f(p_y)$ and $f(p_x)$ for the cases of an initially step-like profile and a profile with gradient. The early evolution of the electron heating is different in the momentum space components p_x and p_y, as shown for the electron distribution densities $f(p_x)$ and $f(p_y)$ in Figs. 10 obtained from the x-p_x and x-p_y phase spaces for a simulation with $k_0 L_g$ =0 and for a 300k_0^{-1} thick target, taken in the interval 200< $k_0 x$ <300 close to tha laser-plasma interface at $k_0 x$ =150 (rear at $k_0 x$ =450). The heating in the p_x component in an first stage occurs in the positive direction until the first hot electrons that arrive at the rear are drawn back from the ambipolar field. For the x interval shown in Fig. 10(a) heated electrons with p_x <0 will therefore note arrive before times $\omega_0 t$ =750 (=150+300+200 with 150 for the rise time of the laser pulse, 300 for the target thickness, and 200 for the return path to the position where $f(p_x)$ is taken). The heating in p_y is from the beginning almost symmetric due to the regular oscillatory character in the laser quiver. As illustrates figure Fig. 11, the bulk of the electron distribution widens slowly in p_y up to times $\omega_0 t$ ∼500, after which, as shows Fig. 12, ultra-relativistic energy tails emerge,

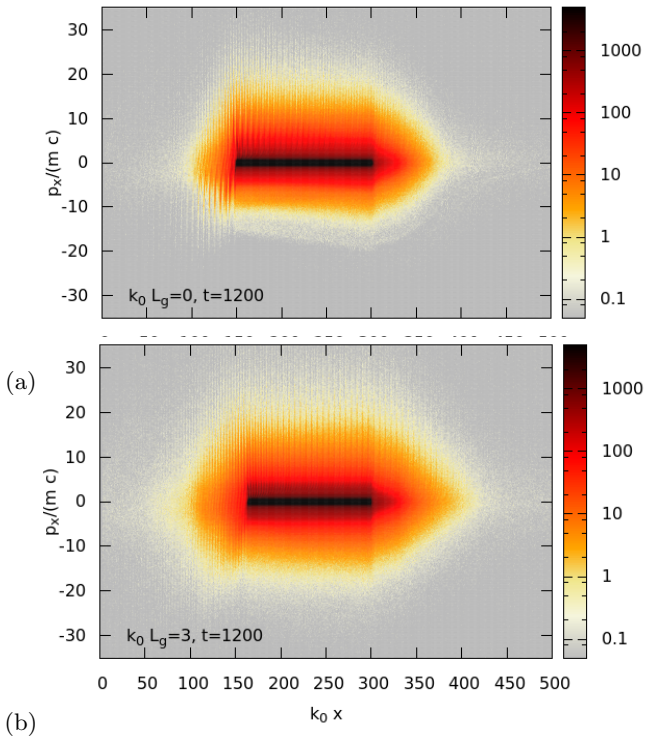

FIG. 9. Phase space contour snap shots in x-p_x, of the entire simulations box, taken at $\omega_0 t$ =1200 for the case of an initially step-like profile (a, top) and for the case of an initially exponential profile $k_0 L_g = 3$ (b, bottom). The color map is highly saturated for >5000 in order to emphasize the population of high energy electrons.

in particular for positive $p_x/m_e c$ values > 10, and later beyond $p_x/m_e c = 20$. This corresponds to what has been observed for stochastic acceleration[16].

For the case of an initially exponential profile, Fig. 11, the widening of the bulk of the electron distribution occurs faster, which apparently goes hand in hand with a faster onset of the ultra-relativistic energy tail in $f(p_x)$, see Fig. 12. Apparently, for similar times, the distributions of the case with an exponential profile produce systematically higher values in the range $|p_x| < 10$, resulting in a more efficient heating of the electron bulk.

The arrival of heated electron at the rear of the target is important for the eventual expansion of the profile there, starting from the moment when heated electron populations dominate the dynamics. The fact that not too short laser pulses continue to heat the plasma from the front side, the particle distribution evolves with a tendency to reinforce the population of energetic electrons.

In a general manner, the distributions show that the dynamics of the electron heating mechanisms for the step-like profile is delayed with respect to profiles with an already developed gradient. The heating is also linked to multi-dimensional effects. In the step-like profile the acceleration of relativistic electrons, ejected due to multi-dimensional effects from the vacuum-plasma interface, and described in Refs. 16–18, and 22, is clearly visible.

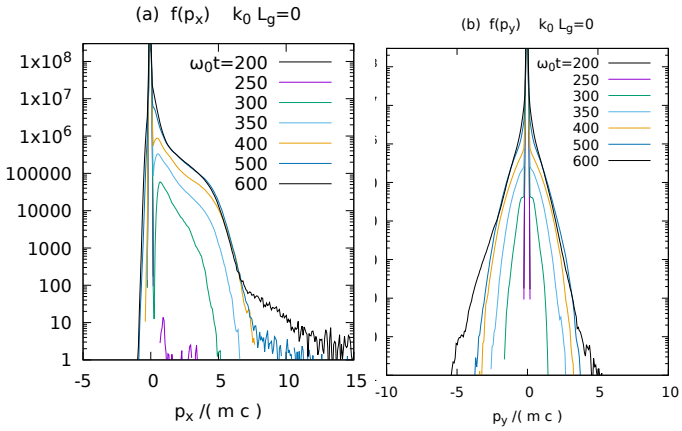

FIG. 10. Electron distribution density $f(p_x)$ (a, left) and $f(p_y)$ (b, right) as a function of the electron momenta p_x and p_y, respectively, at different time instants in the early stage of the interaction taken in the bulk of the plasma (200< $k_0 x$ <300); here for a target of thickness $300 k_0^{-1}$ and for the case with a density profile with a jump between $n_e = 0$ and $n_e = 100 n_c$ at $x = x_c$ (i.e. $k_0 L_g = 0$)

The phase space plot in Fig. 9 also shows that the arrival of ultra-relativistic electrons in bunches, which is therefore not necessarily continuous in time. The formation process of ultra-relativistic electrons, due to stochastic heating in the front part, is present also for the cases with developed gradients but it may initially be masked by the dominant heating of the electron bulk.

E. Characterization of the hot electron distribution

The goal of this section is to characterize the hot electron dynamics in order to eventually link it to the plasma

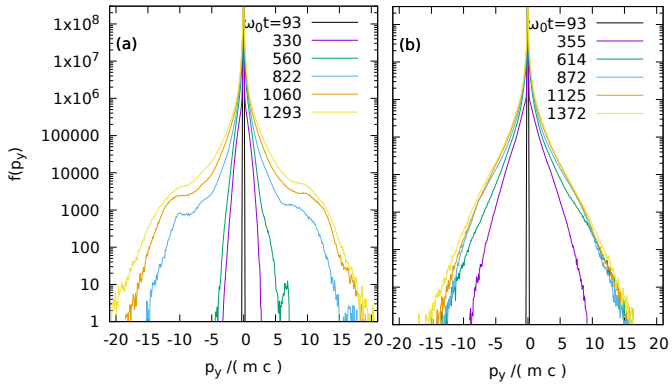

FIG. 11. Electron distribution density $f(p_y)$, at different time instants taken in the bulk of the plasma (130< $k_0 x$ <230), as a function of the electron momentum $p_y/(m_e c)$. (a), left : for a profile with a step-like density profile ($k_0 L_g$ =0); (b), right :for a density profile with a gradient between $n_e = 0$ and $n_e = 100 n_c$ around $x = x_c$ (i.e. $k_0 L_g = 3$).

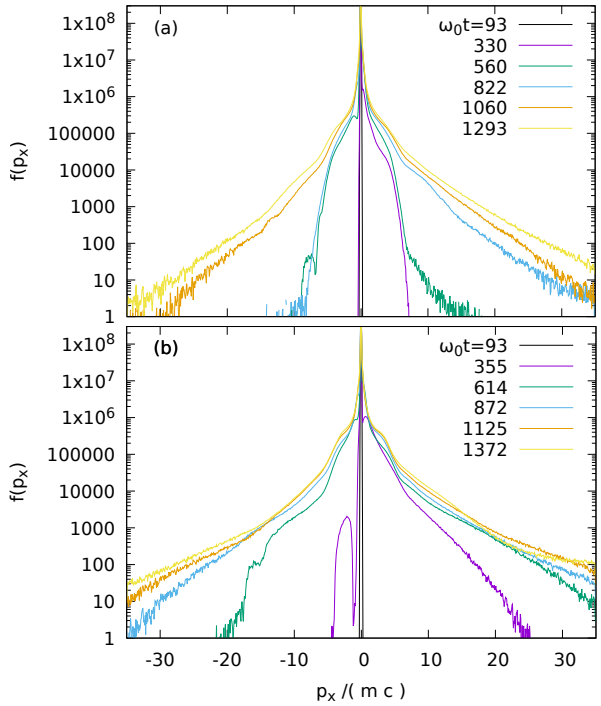

FIG. 12. Electron distribution density $f(p_x)$, at different time instants taken in the bulk of the plasma ($130< k_0x <230$), as a function of the electron momentum $p_x/(m_ec)$. (a), top for k_0L_g =0; (b) bottom for $k_0L_g = 3$.

expansion at the rear of the profile.

The distributions shown in the preceding sub-section show substantial presence of relativistic electrons. For distributions associated with a unique hot electron temperature one can use the relativistic extension of the Gauss/Maxwell distribution, namely the Maxwell-Jüttner (MJ) distribution for which the probability density function (*pdf*) is given characterized by

$$f_{MJ} \propto e^{-\epsilon(\gamma)/k_BT_h} p(\gamma)^{d-1} dp/d\gamma \qquad (2)$$

with $\epsilon(\gamma)/k_BT_h = \gamma/\theta_h$ and $p(\gamma) = (\gamma^2-1)^{1/2}$ considering motion in d dimensions and $dp/d\gamma = (1-1/\gamma^2)^{-1/2}$ and $p = \sqrt{\gamma^2-1}$. For such type of distributions, the resulting expectation values γ_{MJ} and p_{MJ} can be related to the hot electron temperature, namely, for the entire interval $0\leq p < \infty$ ($1 \leq \gamma < \infty$).

For the current case of an almost one-dimensional expansion dynamics at the rear of the target, we consider the motion of hot electrons essentially in positive x-direction so that d =1. The integral for the expectation value γ_{MJ} for γ clearly yields then a relation to θ_h via $\int_{\gamma=1}^{\infty} \gamma\, f_{MJ}(\gamma)d\gamma \equiv \int_{\gamma=1}^{\infty} \exp(-\gamma/\theta_h)\gamma d\gamma/K_1(\theta_h^{-1})$ yielding for the expectation value

$$\gamma_{MJ} = \theta_h + K_0(\theta_h^{-1})/K_1(\theta_h^{-1}) \ , \qquad (3)$$

with K_n denoting the modified Bessel function of the 2nd kind. In the sub-relativistic case, namely $\gamma_{MJ} < 1.4$, the latter expression can be approximated by $\gamma_{MJ} \simeq \theta_h + (1-\theta_h/8)/(1+3\theta_h/8)$. In the ultra-relativistic case, $\gamma_{MJ}^2 \gg 1$ Eq. (2) yields with $dp/d\gamma \to 1$ a purely exponential law for which the integral yields a simple relation to the temperature, namely $\theta_h \simeq \gamma_{MJ} - 1$.

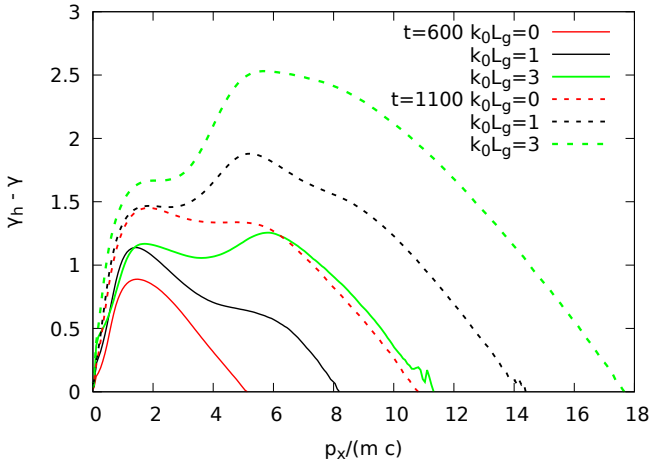

FIG. 13. Difference $\gamma_h(\gamma) - \gamma$ between the expectation value $\gamma_h(\gamma)$, defined in Eq. (4), and γ, for distinct times $\omega_0 t$ =600 (solid lines) and 1100 (dashed). Plateau-like behavior as a function of p_x is develops in the p_x-intervals of $1.5 < p_x/(m_ec) < 2.5$ and $5< p_x/(m_ec) <7$. The value of this difference indicates, for $\gamma^2 \gg 1$ the hot electron temperature over the local p_x interval. The values are deduced from the distribution functions $f(p_x)$ corresponding to the $x-p_x$ phase space over the spatial interval of $100k_0^{-1}$ in the bulk before the rear of the target, for the 3 different density gradients at the front,k_0L_g =0(red lines), 1(black), and 3 (green).

We cannot expect a single hot electron population due to the different acceleration mechanisms at the laser-plasma interface that arise in the simulations. For this reasons we adopt the following strategy to determine an effective temperature from the distributions deduced from our simulations. To detect intervals in p_x and equivalently γ in which hot electron populations develop, we integrate the distribution $f(\gamma)$ such that the obtained value of $\int_{\gamma}^{\gamma_{max}} f(\gamma')d\gamma'$ can be associated with the temperature of an equivalent MJ distribution, as developed in the preceding paragraphs. In the high-energy limit the expression of Eq. (2) yields with $dp/d\gamma \to 1$ a purely exponential law for which the integral with a clear relation to the temperature, namely $N_\gamma \int_{\gamma}^{\infty} \gamma' \exp(-\gamma'/\theta_h)d\gamma' \equiv \gamma + \theta_h$, with $N_\gamma = 1/(\int_{\gamma}^{\infty} f(\gamma')d\gamma')$. The expectation value of the γ value obtained by integration of the distributions over an interval in the positive branch of p_x,

$$\gamma_h(\gamma) \equiv N_\gamma \int_{\gamma}^{\gamma_{max}} \gamma' f(\gamma')d\gamma' \ , \qquad (4)$$

still depends on the lower bound of the integral γ and on the maximum momentum p_{max} registered in the simulations, $\gamma_{max} = \sqrt{1+p_{max}} \gg 1$.

For populations to which a specific 'temperature' θ_h can be associated, the values of $\gamma_h(\gamma)$ exhibit plateau-like behavior over an interval in γ, as seen in Fig. 13. This figure shows the formation of two plateau regions, namely around $p_x/(m_e c) \simeq 1.7$ and 6, i.e. $\gamma \simeq 2$ and 6, respectively. We have consequently determined the hot electron temperatures $\theta_{h,1}$ and $\theta_{h,2}$ for these two electron populations around $\gamma_{h,1}$ =2 and $\gamma_{h,2}$ =6, respectively. Their evolution as a function of time is shown in Fig. 15, respectively, for the cases with $k_0 L_g$ =1,2, and 3 and with a target thickness of $150 k_0^{-1}$. In Fig. 16 the cases with $k_0 L_g$ =1 and 3 are confronted for two different target thickness, namely $150 k_0^{-1}$ and 300 k_0^{-1}. Figure 14 shows the probability densities $f(p_x)$ corresponding to the curves shown in Fig. 13.

To understand the dynamics of the entire electron population, we have also computed the effective hot electron temperature of the entire distribution by performing another integration of γ_h over the electron distribution $f(\gamma)$, see Fig. 14, namely by weighting over different hot electron contributions,

$$\gamma_\theta \equiv N_{\gamma=1} \int_1^{\gamma_{max}} \gamma_h(\gamma') f(\gamma') d\gamma' \ , \qquad (5)$$

again for $\gamma_{max}^2 = 1 + p_{max}^2 \gg 1$. As already mentioned, the value of γ_θ can be estimated as $\gamma_\theta \to \gamma + \theta_h(\gamma_\theta)$ in the relativistic limit, for which MJ distributions are close to an exponential one. The temperature value θ_h can be deduced for the expectation values γ_θ solving Eq. (3) from the Maxwell-Jüttner distribution. An approximate

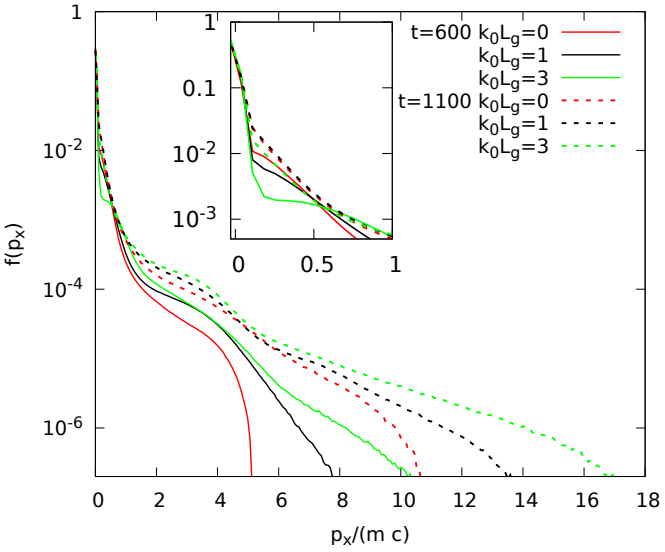

FIG. 14. Distribution density $f(p_x)$ for $p_x \geq 0$ in the interval for times $\omega_0 t$ =600 (solid lines) and 1100 (dashed), deduced from the distribution functions corresponding to the $x - p_x$ phase space in the spatial interval of $100 k_0^{-1}$ in front of the rear of the target, for the 3 cases with different density gradients at the front, $k_0 L_g$ =0 (red line), 1(black), and 3 (green).

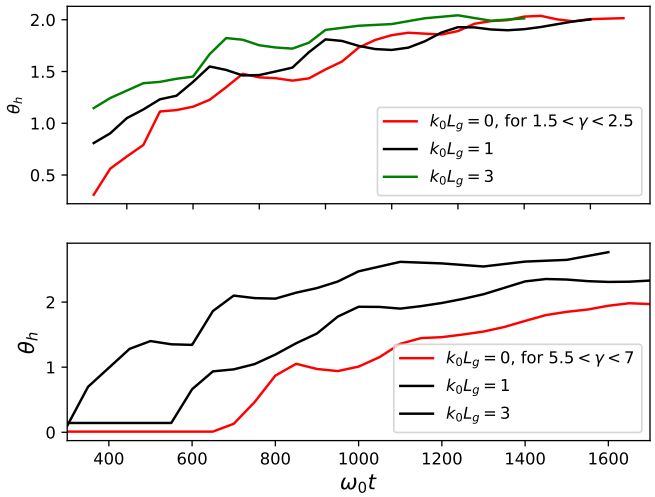

FIG. 15. Hot electron temperatures, $\theta_{h,1}$ and $\theta_{h,2}$, as a function of time, deduced from the expectation values $\gamma_h(\gamma)$, defined in Eq. (4), and γ, as a function of time for distinct values at which plateau-like behavior is seen in Fig. 13, namely around $p_x/(m_e c)$ =1.7, in the upper plot, and $p_x/(m_e c)$ =6 in the lower subplot, . Cases shown are those for the three cases $k_0 L_g$ =0(red), 1(black), and 3 (green). The target thickness for all three cases is $150 k_0^{-1}$.

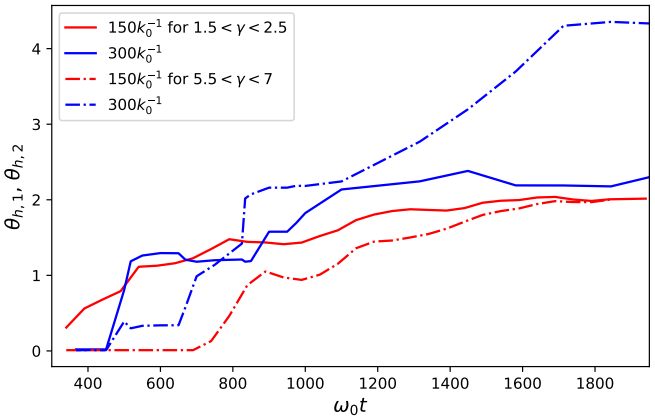

FIG. 16. Hot electron temperatures, $\theta_{h,1}$ and $\theta_{h,2}$, as a function of time, deduced from the expectation values $\gamma_h(\gamma)$, defined in Eq. (4), and γ, as a function of time for distinct values at which plateau-like, namely around $p_x/(m_e c)$ =1.7 (solid lines) and $p_x/(m_e c)$ =6 (dashed). Both cases correspond for the same $k_0 L_g$ =0, but for two different target thicknesses, i.e. $150 k_0^{-1}$ (red) and 300 k_0^{-1} (blue).

explicit expression for γ_θ <1.4 reads $\theta_h(\gamma_\theta) \simeq (\gamma_\theta - 1)/2$. The value of this effective hot electron temperature is computed for the distributions from the simulations for the different cases with $k_0 L_g$ = 0,1, and 3 in Figure 17.

The time behaviors of the temperatures $\theta_{h,1,2}$, seen in Figs. 15 and 16 as well as the value $\theta_h(\gamma_\theta)$ in Fig. 17 associated with Eq. (5) reveal almost periodic phases of heating and stagnation, starting with the arrival of the laser pulse at the laser-plasma interface. Repetitive

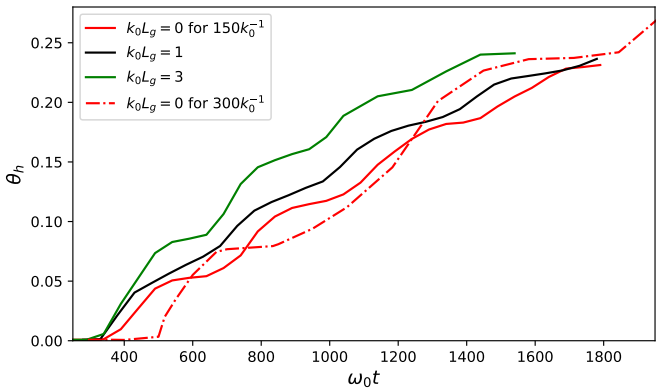

FIG. 17. Hot electron temperature, as a function of time, deduced solving Eq. (3) to obtain θ_h from the expectation value γ_θ from Eq. (5) for the 3 cases with a target thickness of $150k_0^{-1}$ and with different density gradients at the front k_0L_g =0 (red solid line), 1(black) and 3(green), as well as an additional case with k_0L_g =0 (dash-dotted blue line) for a thickness of $300k_0^{-1}$.

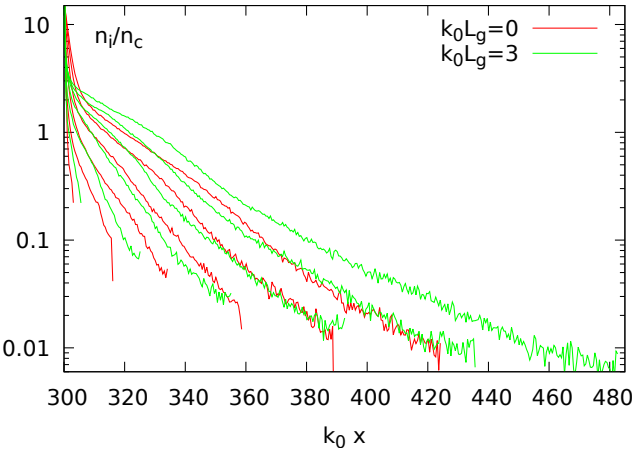

FIG. 18. The ion density profile at the rear of the target for different time instants (from $\omega_0 t$ =300 to 1300 in steps of $\omega_0\Delta t$ =200), showing a comparison between the two cases with a gradient k_0L_g =0 (red lines) and 3 (green lines).

heating arises when hot electrons circulating through the target return to laser-plasma interface where they are re-accelerated. The period of these acceleration phases is related to the target thickness which is seen both in the phases space images $x - p_x$ as well as in Fig. 17 for the value of θ_h. The first onset of heating coincides also with the drop in the reflectivity observed in Fig. 4(a). A difference in the period is clearly seen in comparing the case with the thickness L_t =$300k_0^{-1}$, for k_0L_g =0 with the three cases with different gradients for the thickness L_t =$150k_0^{-1}$. The heating-stagnation phases are separated typically by $2L_t/c$ being $\sim 600\omega_0^{-1}$ and $\sim 1200\omega_0^{-1}$, respectively, which is each time the ballistic circulation time of relativistic electrons. For repeated re-circulation processes this periodicity increases gradually with the increasing dispersion in the length of the trajectory of electrons that are recalled by the ambi-polar field at the rear of the target according to their kinetic energy $\propto (\gamma - 1)$.

F. Expansion of ion and electron profiles at the rear layer

The values of those hot electron temperature are useful for models that describe the hydrodynamic expansion of the ion density profile at the rear of the plasma target. The ion front that forms and moves away from the rear face of the plasma, as seen in Figs. 2(b) and 18, corresponds to effective ion acceleration, and is therefore of potential interest for applications (such as proton diagnostics).

Models have been developed for planar expansion, normal to the rear face in x direction. In the context of laser-plasma interaction the assumption of an isothermal equation of state for the electrons is generally a good approximation, and for this reason most of the studies are based on an isothermal law for the electron dynamics[2,3,26–28] on the slow, ionic time scale. Those models assume the formation of 'cold (co)' and 'hot (h)' populations characterized by their temperatures T_{co}, T_h and densities n_{co}, n_h, respectively, fulfilling $n_i \equiv n_{co}\exp(e\varphi/k_BT_{co}) + n_h\exp(e\varphi/k_BT_h)$, with k_B denoting the Boltzmann constant. In a similar manner, also the rarefaction for the adiabatic case has been considered[29,30].

For the isothermal case in a semi-finite plasma slab the rarefaction can be considered to follow a similarity law[31] such that the spatial coordinate x and time t can be combined to a single similarity variable $x/(c_st) \to \xi + const$ in the set of hydro-dynamic equations for continuity and momentum, with c_s denoting the sound speed of the plasma, $c_s \equiv (ZkT/m_i)^{1/2}$, in which Z is the ion charge. For the ion density with an exponential law, it follows then for advanced times ($c_st \gg v_{th,e}/\omega_{pe,0}$)

$$n_i(x,t) = n_0 e^{-\xi(x,t)} \ , \tag{6}$$

with $\xi \equiv (x - x_r)/(c_st)$, and x_r denoting the position of the rear face of the plasma at $t = 0$. For what concerns the ion front motion, the plasma temperature T is dominated by the hot electron component $k_BT_h \sim \varepsilon_h$. For the case of constant temperature T_h, the resulting ion velocity is given by $v(x,t)/c_s = (x - x_r)/(c_st)$, while for a hot electron temperature 'slowly' evolving in time, the sound speed evolves as well, such that one has to consider to replace c_st by the integral $\int^t c_s dt'$. The balance between the electron pressure and the electrostatic field, $eE_x = -(1/n_e)\partial_x(n_ek_BT_h)$, keeps quasi-neutrality. From Eq. (6) it follows for an isothermal plasma[4]

$$eE_{x,s} = k_BT_h\frac{d\xi}{dx}(x,t) \ . \tag{7}$$

For constant temperature, as assumed in most of the models, this results in $eE_{x,s} = k_BT_h/(c_st)$ or $E_0/(\omega_{pi}t)$

by involving as ω_{pi} the ion plasma frequency (in the unperturbed plasma) of the hot ('h') electron component, $\omega_{pi} \propto n_h^{1/2}$. Equivalently n_h enters then in the field value $E_0 \equiv (n_h k_B T_h/\epsilon_0)^{1/2}$. For advanced expansion, quasi-neutrality can no longer be maintained in the lower shelf. This occurs when in the plasma profile $c_s t$ equals the local Debye length.[4,31] An expression for the evolution of the electric field at the front for all times, assuming fixed values for T_h and n_h, has been given in Ref. 4,

$$E_{x,f} = \frac{2E_0}{\sqrt{2\exp(1) + \omega_{pi}^2 (t-t_r)^2}} \text{ with } t \geq t_r, \qquad (8)$$

with a reference time t_r, discussed later.

This process has been extensively studied, also with better precision concerning the expression for the ion front. These models assume the (hot) electron temperature as an initial value, but do not consider that the heating is maintained from the front side. For the case of ongoing heating (or eventual cooling) of the hot electron population, Eq. (7) can be generalized resulting in

$$eE_{x,s} = \frac{k_B T_h(t)}{\int^t c_s(t')dt'}, \qquad (9)$$

provided that the temporal change in T_h is not too fast, and that the self-similar character of the solution is preserved and that similarity variable ξ is associated with a monotonous evolution along the path $\int^t c_s dt'$.

G. Ion front dynamics

The accelerating electrostatic field that governs the ion front motion can be integrated in time, for which v_f and x_f mark the front of the ion profile, beyond which electron cloud has formed.

Both v_f and x_f result by simple integration of the equations of motions

$$\frac{dv_f}{dt} = \frac{Z}{m_i} E_{x,f} \quad \text{and} \quad \frac{dx_f}{dt} = v_f \ . \qquad (10)$$

To examine the range of validity of previous models, it is of interest to consider the case of increasing hot electron temperature in the plasma slab due to the arrival of hot electrons accelerated at the front vacuum (preplasma)- dense plasma interface.[4,27,28,32]. With the help of the expression for the isothermal rarefaction, Eq. (6) and Eq. (9), one has consequently to relate the value of the accelerating electric field to the expansion such that Eq. (8) has to be replaced by

$$\frac{eE_{x,f}}{m_e\omega_0 c} = \frac{2\theta_h(t)}{\sqrt{2\mathrm{e}^1 \frac{n_c}{n_h}\theta_h + (\int_{t_r}^t k_0 c_s(\theta_h)dt')^2}} \ , \qquad (11)$$

wherein n_h denotes the density of the hot electron population and in which the ion sound speed is related to the hot electron temperature via $c_s(\theta_h)/c = \sqrt{\theta_h m_e/m_i}$, being a function of time. The first term in the denominator accounts only for the initial value of $E_{x,f}$ while the long time behavior is clearly dominated by the self-similar expansion, $eE_{x,f}/(m_e\omega_0 c) \to 2\theta_h(t)/\int\sqrt{\theta_h(t')m_e/m_i}\omega_0 dt'$.

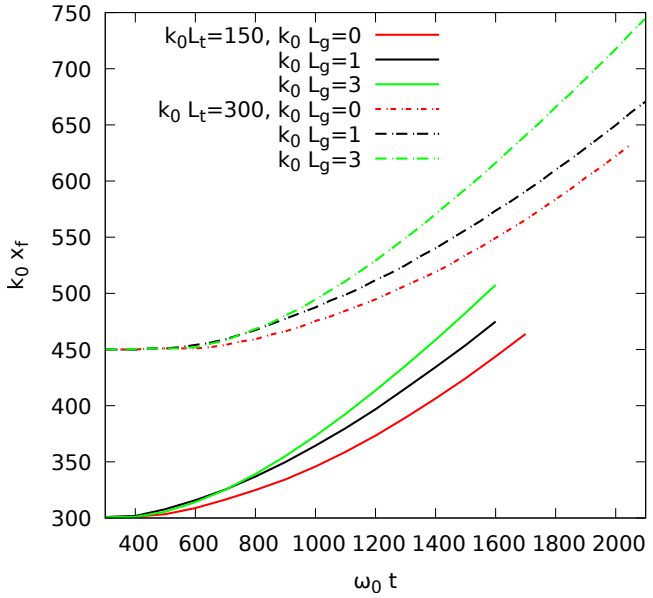

FIG. 19. Time evolution of the ion front position x_f behind the target as a function of time, for both target thicknesses, 150 (solid lines) and $300k_0^{-1}$ (dash-dotted), for the three cases with gradients k_0L_g =0(red), 1(black), and 3(green lines).

It is therefore essential to understand which hot electron population governs the acceleration process.

The dynamics of the ion front described by Eqs. (10) lead to profile expansions shown in Fig. 18 for a series of time instants, and for two cases, a step-like (red lines) interface and an interface with finite gradient (green for $k_0L_g = 3$). The profiles exhibit a sharp ion front that decreases in density with time. The electron profiles, not shown here follow essentially the part almost up to the front, while their profiles are naturally extended to higher x-values without a sharp front due to the large diffusion of electron energies. From the ion profiles one can conclude that there is a temporal delay between both cases, which is related to the acceleration process of the hot electron populations.

This is confirmed in the curves of Fig. 19 and for the time evolution of the ion fronts, deduced from the values in Fig. 18 for all three cases (again red for step-like, black and green for exponential, k_0L_g =1, and 3, respectively). In spite of the difference of the distribution functions, apart from the time delay due to the different target thickness, the behaviours are very similar. As a matter of fact, the case with the weakest gradient, $k_0L_g = 3$, leads to a more efficient acceleration at the laser-plasma interface, so that the rear expansion is faster. We have determined the spatial profiles of the electric fields E_x for several time instants, shown in Figs. 20 for the cases with k_0L_g =0,1, and 3, respectively and for a target of the thickness $150k_0^{-1}$, in which the electric field $E_{x,f}$, as-

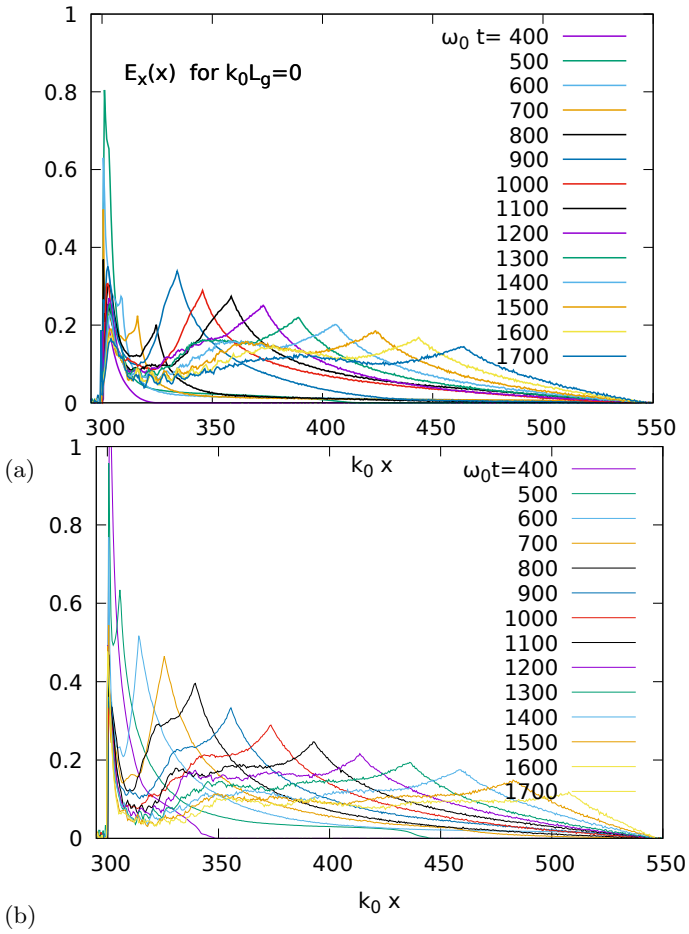

FIG. 20. Spatial profiles, in x, of the electric field $eE_x/(m_e\omega_0 c)$ at the rear side of the target for a sequence of time instants (in steps of $100\omega_0^{-1}$), for the case of target thickness of $150k_0^{-1}$, and for the cases with the gradient k_0L_g =0 (a, upper plot) and k_0L_g =3 (b, lower).

sociated with the accelerated ion front, is associated with the pronounced peak. Its position moves in time so that we have deduced the time evolution of $E_{x,f}$ for each case, which is shown in Fig. 22 for the thickness $300k_0^{-1}$ and in Fig. 21 for the cases of $150k_0^{-1}$.

The temporal evolution of the electric field $E_{x,f}(t)$ deduced from the simulations shows in Figs.21 and in 22 a non-monotonous descent in time, which is a reminiscence of the contribution of successive hot electron populations, as seen in Figs. 15 and 16. We have therefore compared the values shown in Figs. 21 and 22 with the model of Eq. (11), for advanced times, in using the hot electron temperatures $\theta_{h,1}$ and $\theta_{h,2}$ deduced from the electron distribution functions. The evolution of $\theta_{h,1}(t)$ and $\theta_{h,2}(t)$ are delayed in time for both steeper interfaces, k_0L_g =0 and 1, so that $\theta_{h,1}$ governs the motion up to the moment when re-accelerated electrons heat the target bulk, hence $\omega_0 t$ >600 for k_0L_t =150. This explains an almost abrupt increment of $E_{x,f}$ around $\omega_0 t$ ∼800, seen in Fig. 21. For the case k_0L_g =3 the onset of both hot electron populations is not particularly delayed so that the increment in $E_{x,f}$ is less pronounced.

To model the behavior of $E_{x,f}$ based on the deduced $\theta_{h,1,2}$ values, we have chosen, for the simplicity, to define θ_h in Eq. (11) by the sum of both hot electron temperatures $\theta_h(t) = \theta_{h,1}(t) + \theta_{h,2}(t)$. The latter gives the best agreement with the values deduced from the profiles, see comparison between Figs. 21 (a) and (b) respectively The agreement found confirms that, first, the hot electron population with kinetic energies $\sim \gamma - 1$ in the interval 1.5< γ <2.5 govern the rear plasma expansion, while, later on, the electrons of the hotter electron population take over this role. The temperature evolution shown in Fig. 17 indicates the heating of the bulk electrons, but cannot explain the rear expansion. From the speed of

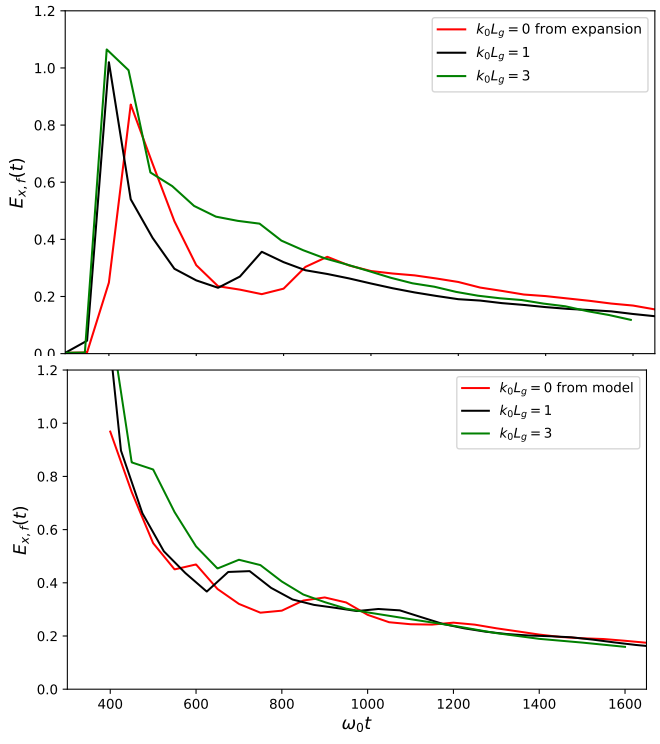

FIG. 21. Time evolution of the (normalized) electric field $eE_{x,f}/(m_e\omega_0 c)$ at the ion front position behind the target as a function of time, for the case of target thickness of $150k_0^{-1}$. The upper subplot (a) shows a comparison between values deduced from the expansion as in Fig. 20; in (b), below are shown the values deduced from the model of Eq. (11) in applying the values of $\theta_h(t) = \theta_{h,1}(t) + \theta_{h,2}(t)$ from the electron distribution functions. Cases shown are with an abrupt jump at the front (red lines), and gradients k_0L_g =1 and 3 (black and green lines).

the ion front evolution, shown in Fig. 23, one can deduce the ion speed and the corresponding ion energy of the ions in the front. The values, for both cases, reach eventually $v_f/c \sim 0.2 \ldots 0.25$ which corresponds to ion (here proton) energies in the range of 18-30 MeV.

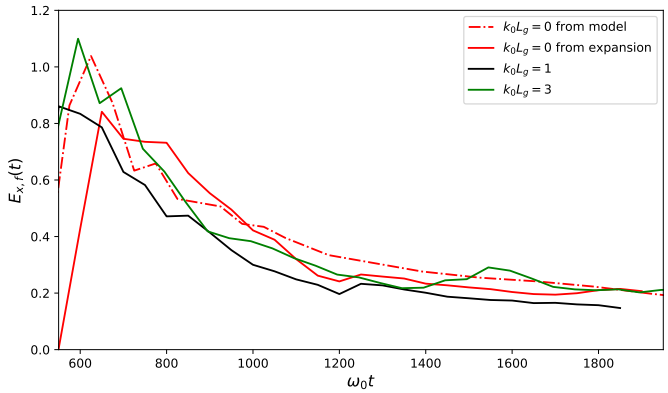

FIG. 22. Time evolution of the electric field $eE_{x,f}/(m_e\omega_0 c)$ at the ion front as a function of time, for the case of target thickness of $300k_0^{-1}$, and for the three cases with gradients k_0L_g =0 (red), 1, and 3 (black and green lines). The values obtained from the model Eq. (11) with $\theta_h(t) = \theta_{h,1}(t)+\theta_{h,2}(t)$ are shown as comparison for the case k_0L_g =0

III. DISCUSSION AND CONCLUSIONS

We have examined the acceleration of electrons and ions by laser interaction with a dense plasma with steep interfaces where the laser beam impinges on the plasma target. In particular we have studied the sensibility of electron acceleration and heating mechanisms on the gradient of a pre-formed plasma, in focusing on the dynamics normal to direction of incidence. Finite gradients may originate from pre-formed plasma by a long time-scale foot ('pièdestal') of a short laser pulse with insufficient contrast, by a preceding heater beam, or by disintegration of a pre-imprinted surface structure of specially prepared target plasmas, in spite of possible profile steepening. Our simulations have been carried out with the particle-in-cell code EMI2D in 2 spatial and 3 dimensions in velocity. Most of our shown results focus on the motion in the direction of the incoming laser light. It is however important to mention that the motion across the laser propagation is important. Simulations in only 1D cannot show the essential mechanisms for acceleration because the action of the laser ponderomotive potential blocks the motion in this only direction. In 2D or 3D the shape of the electromagnetic fields become modulated due to self-focusing/filamentation. We have limited our study to an initially plane wave field, ignoring the transversal spatial shape of a focused beam, that eventually may lead to hole boring. We believe, however, that focusing and hole boring effects introduce additional parameters that do not help to find a better interpretation at this stage.

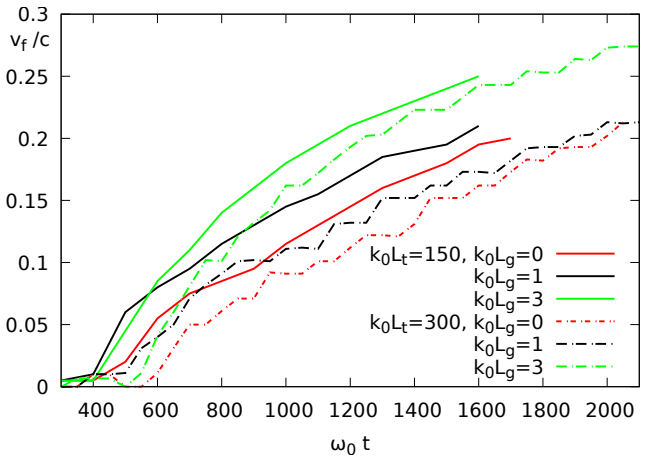

FIG. 23. Time evolution of the ion front velocity v_f behind the target as a function of time, for both target thicknesses, 150 (solid lines) and $300k_0^{-1}$ (dash-dotted), showing a comparison between the three cases with gradients k_0L_g =0(red), 1(black), and 3(green lines).

We have also carried out simulations at higher laser intensity, and different sizes of the plasma. The cases shown here for the reference parameters with $a_0 = 2.8$ and the chosen plasma size, are quite representative for the obtained results. For the cases with $a_0 = 2.8$, the resulting ion front motion attains eventually proton energies of 15-30MeV.

As mentioned above, the duration of our simulations was up to 200-250 laser oscillation cycles (up to $500fs$), assuming constant laser intensity after a ramp in time. It should be remarked that the physics of the acceleration processes is considerably different as long as the laser pulse duration does not allow, as e.g. in Ref. 8, the formation of a sufficiently extended standing wave structure due to the superposition of the incident and reflected light in front of the plasma. Although we have considered steep gradients from $k_0L_g = 0$ to $= 3$, the mechanisms in play prove to change already in this range of L_g with respect to the electron dynamics in the incident and reflected laser-light fields in front of the plasma. Ponderomotive profile steepening stabilize the profiles, but only in the vicinity of the critical density. For those gradients, the motion of electrons, once ejected from the steep gradient interface, is dominated by the standing wave structure of the light fields due to still strong reflection. For step-like profiles, the acceleration of relativistic electrons by stochastic motion in the standing wave structure is important. Such electrons can then propagate through the dense plasma without that their motion is too much affected (depending on the target thickness). This process is also present for finite gradients, but the ponderomotive-type acceleration of the bulk of electrons becomes predominant, leading to a heating of the electron bulk at earlier times. The formation of hot electron populations arises via re-circulation of electron through the target such that they get re-accelerated each time when arriving at the laser-plasma interface. For the cases shown two populations of electrons form a sub-distributions, here around $p_x/(m_e c)$ ∼1.7 and 6, with their associated hot electron temperature that increases in time via heating and stagnation phases.

The analysis of the expansion of ion profiles at the

rear of the target shows that its dynamics can still be associated with theoretical models based on self-similar expansion, in considering that the arising electron population contribute. For experiments for which diagnostics of hot electron populations a link with modelling can therefore be envisaged. Changes in the acceleration dynamics depend on the laser pulse duration τ_p with respect to the ballistic re-circulation time of relativistic electrons through the target, $2L_t/c$.

ACKNOWLEDGMENTS

The simulations were granted access to the French HPC resources of IDRIS under the allocation AD010500573R1 made by GENCI, France. We also thank the CPHT computer team.

[1] L. M. Wickens, J. E. Allen, and P. T. Rumsby, Phys. Rev. Lett. **41**, 243 (1978).
[2] M. A. True, J. R. Albritton, and E. A. Williams, Physics of Fluids **24**, 1885 (1981).
[3] J. E. Crow, P. L. Auer, and J. E. Allen, Journal of Plasma Physics **14**, 65–76 (1975).
[4] P. Mora, Phys. Rev. Lett. **90**, 185002 (2003).
[5] A. Gurevich, D. Anderson, and H. Wilhelmsson, Phys. Rev. Lett. **42**, 769 (1979).
[6] V. F. Kovalev, V. Y. Bychenkov, and V. T. Tikhonchuk, Journal of Experimental and Theoretical Physics **95**, 226 (2002).
[7] V. F. Kovalev and V. Y. Bychenkov, Phys. Rev. Lett. **90**, 185004 (2003).
[8] V. Y. Bychenkov, V. N. Novikov, D. Batani, V. T. Tikhonchuk, and S. G. Bochkarev, Physics of Plasmas **11**, 3242 (2004).
[9] V. T. Tikhonchuk, A. A. Andreev, S. G. Bochkarev, and V. Y. Bychenkov, Plasma Physics and Controlled Fusion **47**, B869 (2005).
[10] A. Héron, J. C. Adam, and P. Mora, Physics of Plasmas **27**, 013103 (2020), https://doi.org/10.1063/1.5127164.
[11] J. S. DeGroot and J. E. Tull, The Physics of Fluids **18**, 672 (1975), https://aip.scitation.org/doi/pdf/10.1063/1.861216.
[12] B. Bezzerides, S. J. Gitomer, and D. W. Forslund, Phys. Rev. Lett. **44**, 651 (1980).
[13] F. Brunel, Phys. Rev. Lett. **59**, 52 (1987).
[14] A. J. Kemp, Y. Sentoku, and M. Tabak, Phys. Rev. E **79**, 066406 (2009).
[15] C. Thaury, P. Mora, A. Héron, and J. C. Adam, Phys. Rev. E **82**, 016408 (2010).
[16] S. Hüller, A. Porzio, J.-C. Adam, and A. Héron, Physics of Plasmas **26**, 083107 (2019), https://doi.org/10.1063/1.5111934.
[17] Z.-M. Sheng, K. Mima, Y. Sentoku, M. S. Jovanović, T. Taguchi, J. Zhang, and J. Meyer-ter Vehn, Phys. Rev. Lett. **88**, 055004 (2002).
[18] Z.-M. Sheng, K. Mima, J. Zhang, and J. Meyer-ter Vehn, Phys. Rev. E **69**, 016407 (2004).
[19] G. Blaclard, F. Quéré, G. Bonnaud, and H. Vincenti, Phys. Rev. E **107**, 034205 (2023).
[20] D. F. Escande and F. Doveil, Journal of Statistical Physics **26**, 257 (1981).
[21] G. Schmidt, Comments Plasma Phys. Controlled Fusion **7**, 87 (1982).
[22] J. May, J. Tonge, F. Fiuza, R. A. Fonseca, L. O. Silva, C. Ren, and W. B. Mori, Phys. Rev. E **84**, 025401 (2011).
[23] S. Wilks and W. Kruer, IEEE Journal of Quantum Electronics **33**, 1954 (1997).
[24] R. Mishra, Y. Sentoku, and A. J. Kemp, Physics of Plasmas **16**, 112704 (2009), https://doi.org/10.1063/1.3249691.
[25] S. V. Bulanov, A. Yogo, T. Z. Esirkepov, J. K. Koga, S. S. Bulanov, K. Kondo, and M. Kando, Physics of Plasmas **22**, 063108 (2015), https://doi.org/10.1063/1.4922679.
[26] J. S. Pearlman and R. L. Morse, Phys. Rev. Lett. **40**, 1652 (1978).
[27] A. Diaw and P. Mora, Phys. Rev. E **84**, 036402 (2011).
[28] A. Diaw and P. Mora, Phys. Rev. E **86**, 026403 (2012).
[29] T. Kiefer and T. Schlegel, Physics of Plasmas **19**, 102101 (2012), https://doi.org/10.1063/1.4754863.
[30] C. Thaury, P. Mora, J. C. Adam, and A. Héron, Physics of Plasmas **16**, 093104 (2009), https://doi.org/10.1063/1.3206940.
[31] P. Mora and R. Pellat, The Physics of Fluids **22**, 2300 (1979), https://aip.scitation.org/doi/pdf/10.1063/1.862541.
[32] P. Mora and T. Grismayer, Phys. Rev. Lett. **102**, 145001 (2009).